Passivity-Based Model Predictive Control of Three-Level Inverter-Fed Induction Motor

Fengxiang Wang, *Senior Member, IEEE*, Guiying Lin, and Yingjie He, *Student Member, IEEE*

***Abstract*—Finite control set model predictive control (FCS-MPC) of three-level neutral point clamped inverter-fed induction motor has received wide concern recently, thanks to its low switching frequency and fast dynamics. However, the performance largely depends on the accurate measurement and parameters which determine the feedback and control loops, respectively. Besides, FCS-MPC demands a large number of resources to perform the exhaustive search, which indicates that the computation burden increases exponentially with the increasing switching states. Aiming at improving the robustness under the condition of unavoidable measuring noises and parameter variation as well as reducing the computational burden, a passivity-based model predictive control (PB-MPC) scheme is presented in this article. For an ideal system, the PB-MPC has a similar character as that of the FCS-MPC. In real applications, where noises and disturbances impact the system more or less, PB-MPC outperforms FCS-MPC due to the power shaping and damping injection inherited from passivity-based control which ensures the asymptotic stability. A Lyapunov function is designed to prove the stability of the proposed scheme. The stability and efficiency are verified by both simulation and experimental results.**

***Index Terms*—Induction motor (IM), model predictive control (MPC), passivity-based control (PBC), three-level neutral point clamped converter.**

I. Introduction

NEUTRAL point clamp (NPC) converters are characterized by low switching frequency, low distortion factor, and low voltage drop, which makes NPC converters suitable for medium- and high-power situations [1], [2]. In NPC inverter-fed induction motors (IMs), the flux and torque take essential parts in the control target, along with the neutral point potential which is a fundamental element in NPC converters [3]. Finite control set model predictive control (FCS-MPC) strategies which have been applied to many systems, e.g., back-to-back (BTB) converter for wind turbine [4], active front-end (AFE) [5], and Z-source inverter [6], are capable of handling additional constrains including neutral point voltage without much effort by searching the optimal vector from the candidates [7].

Among the predictive strategies in alternating-current (ac) motors, predictive torque control (PTC) and predictive current control (PCC) are the most well-known schemes [8]. PTC is characterized by its fast speed, while the current total harmonic distortions (THDs) of PTC are higher than PCC [9]. Literature [10] proposed a scheme that obtains a current performance similar to PCC without the knowledge of the rotational angle. PTC that considers maximum torque per ampere in a flux-limited and flux-increased region with little computation effort is proposed in [11]. A robustness MPC scheme for the three-level NPC BTB converter with permanent magnet synchronous generator (PMSG) is presented in [12]. Omitting the calculation of the torque and flux which involves the square root operation, PCC reduces a lot of calculation time. The implementation of PCC in the Vienna rectifier with PMSG system is exploited in [13]. A sensorless PCC based on Luenberger observer is proposed in [14] whose aim is to enhance the robustness.

An issue that impedes the development of FCS-MPC in the real application is the heavy calculation burden during the enumeration of all admissible voltage vectors (VVs) [15]. The processor requires eight exhaustive searches for two-level converters. In the three-level situation, however, a total of 27 iterations are demanded to search all the candidates.

Some studies have investigated the solution to reduce computation time. A simplified MPC scheme was proposed to reduce the computational burden without deteriorating the control performance in two- and three-level AFEs [16]. Literature [17] extended the use of simplified MPC to applications of BTB converter with PMSG. However, the current performance is slightly deteriorated. The above schemes follow the dead-beat (DB) to select the section where the candidates locate in. In [18] and [19], table-based methods are proposed to reduce the computational effort for two-level inverter-fed IM and matrix converter (MC) fed permanent magnet synchronous motor (PMSM), respectively. However, stability issue in these papers is not discussed. Table I shows the detailed comparison.Disturbances from every corner affect the performance of the controller to some extent. Paper [8] explores the sensitivity of FCS-MPC to parameter

Manuscript received October 11, 2019; revised April 20, 2020; accepted June 28, 2020. Date of publication July 13, 2020; date of current version September 22, 2020. This work was supported in part by the National Natural Science Foundation of China under Grant 51877207, in part by the Science and Technology Program of Fujian under Grants 2019T3021, 2018T3015, 2018H2001, and KFJSTS-QYZX-025, in part by the Science and Technology Program of Quanzhou under Grant 2018C097R, and in part by the Program of Haixi Institutes under Grant CXZX-2018-Q01. Recommended for publication by Associate Editor J. Rodriguez. *(Corresponding author: Fengxiang Wang.)*

Fengxiang Wang is with the National local joint Engineering Research Center for Electrical Drives and Power Electronics, Quanzhou Institute of Equipment Manufacturing, Haixi Institutes, Chinese Academy of Sciences, Jinjiang 362200, China (e-mail: fengxiang.wang@fjirsm.ac.cn).

Guiying Lin is with the College of Electrical Engineering and Automation, Fuzhou University, Fuzhou 350108, China (e-mail: lgy2863680500@163.com).

Yingjie He is with the Institute for Electrical Drive Systems and Power Electronics, Technische Universitaet Muenchen, 80333 Munich, Germany (e-mail: yingjie.he@tum.de).

Color versions of one or more of the figures in this article are available online at http://ieeexplore.ieee.org.

Digital Object Identifier 10.1109/TPEL.2020.3008915

TABLE I
ONE-STEP ONE-VECTOR COMPUTATIONALLY EFFICIENT MPC SCHEMES

Ref.	Dead-beat-based approach [16] based on TMS320F28335	Dead-beat-based approach [17] based on NI-CRIO 9082	Table-based approach [18] based on DS1104 R&D	Table-based approach [19] based on TMS320F2812
Pros	Common mode voltage considered Two- and three-level AFE Execution time reduction: Two-level:48.8%,three-level:43.1%	Two candidate region types Three-level BTB with PMSG Execution time reduction: Hexagon:55.1%,Triangle:79.6%	Switching frequency reduction Cost function simplification Execution time reduction: 29.6%	Bi-direction energy flow MC-fed PMSM Execution time reduction: 40.17%
Cons	Front-end only	Slight performance deterioration	Two-level only	Performance deterioration

deviation. Designing a disturbance observer is an effective way to compensate for some disturbances in control schemes. An active disturbance rejection-based MPC is proposed in [20] to reduce the error caused by deviated parameters. An extended state observer for AFEs [21] intends to enhance the robustness against the parameter inaccuracy.

However, errors caused by measuring noises cannot be included in the observed disturbance and high precision sensors are financially expensive. It is important to design a less-expensive scheme in both computation and finance that guarantees the performance in a hostile environment.

Passivity-based control (PBC), which manipulates the power of a dissipation system, ensures asymptotic stability [22]. The stability of the switched reluctance-based wind system can be improved by suppressing the oscillations [23]. Different response periods can be achieved in boost converter by algebraic designing of the damping factor [24].

In this article, a passivity-based model predictive control (PB-MPC) algorithm is proposed to enhance stability and reduce the computational effort. Simulation and experimental results on three-level NPC converter-fed IM further validate the effectiveness of this scheme.

The contributions of this article include the following.

1) An efficient solution to reduce the computational burden of FCS-MPC is proposed.
2) The stability of the proposed scheme is proved by the Lyapunov function.
3) Current and torque performance is improved due to the reduction of the impacts led by the disturbance, which is validated both by simulation and experimental results.

This article is constructed as follows. In Section II, models of three-level NPC converter and IM are established. In Section III, the passivity-based controller and model predictive controller are to be described succinctly based on the model formulated in the previous section. Section IV presents the proposed PB-MPC strategy. Its stability and efficiency are demonstrated via the Lyapunov function and qualitative evaluation in Section V, respectively. Simulation and experimental results are exhibited in Section VI. Finally, article is concluded with Section VII.

The subscripts C_α and C_β in this article denote the α and β elements of array vector $\boldsymbol{C}$ in the stationary frame, respectively, and superscripts $\boldsymbol{C}^*$, $\boldsymbol{C}^p$, and $\hat{\boldsymbol{C}}$ present reference, predictive, and estimated counterparts of $\boldsymbol{C}$, respectively.

II. MODEL OF THREE-LEVEL NPC CONVERTER-FED IM

In this section, the model of the NPC converter-fed IM will be described and the next step value of manipulated variables will be updated based on the model derived. The definition of variables can be referred to in Table II and Fig. 1.

TABLE II
SYSTEM VARIABLES AND PARAMETERS

Description	Parameter	Value
DC-link Voltage	V_{dc}	540 V
DC-link Capacitance	C	4700 μF
Rated Power	P^N	4 kW
Rated Voltage	U^N	380 V
Rated Current	I^N	8.9 A
Rated Rotor Flux	$\|\boldsymbol{\psi}_r\|^N$	0.85 Wb
Rated Torque	T_e^N	26 N·m
Rated Speed	ω_m^N	1445 RPM
Based Frequency	f^N	50 Hz
Pole Pairs	N_p	2
Magnetizing Inductance	L_m	154.7 mH
Stator Inductance	L_s	160.4 mH
Rotor Inductance	L_r	160.4 mH
Stator Resistance	R_s	1.258 Ω
Rotor Resistance	R_r	1.030 Ω
Inertia	J	0.0025 Kg·m^2
Sampling Time	T_s	50 μs

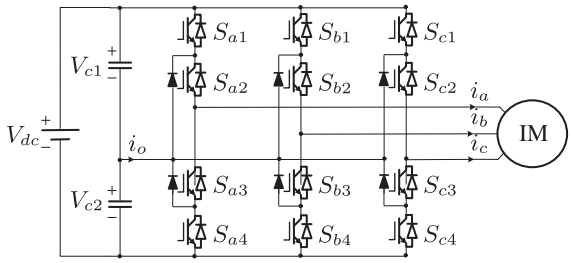

Fig. 1. Three-level NPC converter with IM.

A. Three-Level NPC Inverters

The three-level NPC converter takes its name from the clamping diodes which provide an additional zero voltage level. Assigning the first and fourth power devices in one bridge as S_{x1} and S_{x4}, the switching state of this phase is $S_x = S_{x1} - S_{x4}$, where $x \in \{a, b, c\}$ presents each phase of the power converter. With the switching states of each phase, the VV generated by the NPC converter can be calculated as

$$\boldsymbol{v}_s = \frac{V_{\rm dc}}{2}\frac{2}{3}\begin{bmatrix} 1 & -\frac{1}{2} & -\frac{1}{2} \\ 0 & \frac{\sqrt{3}}{2} & -\frac{\sqrt{3}}{2} \end{bmatrix}\boldsymbol{S} \tag{1}$$

where $\boldsymbol{S} = \begin{bmatrix} S_a & S_b & S_c \end{bmatrix}^T$ is a vector defined in the abc plane.

The capacitor voltages V_{c1} and V_{c2} are controlled by the currents that flow in and draw out. When the $V_{\rm dc}$ is provided by direct-current (dc) voltage source, the only element that affects the capacitor voltage is the neutral point current i_o. The voltage difference ΔV can be expressed as

$$C\frac{d}{dt}\Delta V = C\frac{d}{dt}\left(V_{c1}-V_{c2}\right) = i_o = -\boldsymbol{i}_{abc}^T\cdot \text{abs}(\boldsymbol{S}) \tag{2}$$

where $\boldsymbol{i}_{abc} = [i_a \quad i_b \quad i_c]^T$ is three-phase current in the abc frame and $\text{abs}(\boldsymbol{S}) = [|S_a| \quad |S_b| \quad |S_c|]^T$.

B. Induction Motors

A squirrel-cage IM whose rotor winding is short circuit acts as an ac load of the NPC inverter.

IM can be concluded by the widely accepted mathematical model in the $\alpha\beta$ frame with stator voltage $\boldsymbol{v}_s$ and load torque T_l input. The system states are stator current $\boldsymbol{i}_s$, rotor flux $\boldsymbol{\psi}_r$, and mechanical speed ω_m

$$\sigma L_s\frac{d}{dt}\boldsymbol{i}_s = \boldsymbol{v}_s - R_\sigma \boldsymbol{i}_s + k_r\left(\frac{1}{\tau_r}\boldsymbol{I}_2 - \omega_e\boldsymbol{J}_2\right)\boldsymbol{\psi}_r \tag{3a}$$

$$\frac{T_r}{L_m}\frac{d}{dt}\boldsymbol{\psi}_r = \boldsymbol{i}_s - \frac{1}{L_m}\boldsymbol{\psi}_r + \frac{\omega_e T_r}{L_m}\boldsymbol{J}_2\boldsymbol{\psi}_r \tag{3b}$$

$$J\frac{d}{dt}\omega_m = -T_l - B\omega_m + \underbrace{\frac{3}{2}\frac{L_m}{L_r}N_p\left(\boldsymbol{\psi}_r\times\boldsymbol{i}_s\right)}_{T_e} \tag{3c}$$

where $\boldsymbol{J}_2 = \left[\begin{smallmatrix}0 & 1\\ -1 & 0\end{smallmatrix}\right]$, identity matrix $\boldsymbol{I}_2 = \text{diag}(1,1)$, and $\sigma = 1-\frac{L_m^2}{L_sL_r}$, $k_r = \frac{L_m}{L_r}$, $R_\sigma = R_s + k_r^2R_r$, $\tau_r = \frac{L_r}{R_r}$. Electrical speed $\omega_e = N_p\omega_m$ and electromagnetic torque T_e is proportional to the cross product of rotor flux $\boldsymbol{\psi}_r$ and $\boldsymbol{i}_s$.

III. Model Predictive Control and Passivity-Based Control

Both MPC and PBC serve as the inner loop. Flux reference $\|\boldsymbol{\psi}\|^*$ is set to its rated value and a proportional–integral (PI) controller provides the torque reference T_e^*.

For the current controller, the reference currents on the $\alpha\beta$ frame are obtained from the reference on the dq frame which are calculated with the information of flux and torque reference, by inverse park transformation

$$i_{sd}^* = \frac{\|\boldsymbol{\psi}_r\|^*}{L_m} \tag{4a}$$

$$i_{sq}^* = \frac{2}{3}\frac{L_r}{L_m}\frac{T_e^*}{N_p\|\boldsymbol{\psi}_r\|} \tag{4b}$$

$$\begin{bmatrix} i_{s\alpha}^* \\ i_{s\beta}^*\end{bmatrix} = \begin{bmatrix}\cos(\theta) & -\sin(\theta)\\ \sin(\theta) & \cos(\theta)\end{bmatrix}\begin{bmatrix} i_{sd}^* \\ i_{sq}^*\end{bmatrix} \tag{4c}$$

where the rotation angle θ is obtained from the rotor flux $\boldsymbol{\psi}_r$.

A. Model Predictive Control

MPC, known as receding horizon control, solves the optimization problem by searching within the admissible VVs to find the optimal one that minimizes the cost function.

By discretizing (3), we can obtain the following equations:

$$\begin{aligned}\boldsymbol{i}_s(k+1) = {}& \frac{T_s}{\sigma L_s}\boldsymbol{v}_s(k) + \left(1-\frac{T_sR_\sigma}{\sigma L_s}\right)\boldsymbol{i}_s(k)\\ &+ \frac{T_sk_r}{\sigma L_s}\left(\frac{1}{\tau_r}\boldsymbol{I}_2 - \omega_e\boldsymbol{J}_2\right)\hat{\boldsymbol{\psi}}_r(k)\end{aligned} \tag{5}$$

$$\begin{aligned}\hat{\boldsymbol{\psi}}_r(k+1) = {}& T_s\left(\frac{L_m\boldsymbol{i}_s(k) - \hat{\boldsymbol{\psi}}_r(k)}{\tau_r} + \omega_e\boldsymbol{J}_2\hat{\boldsymbol{\psi}}_r(k)\right)\\ &+ \hat{\boldsymbol{\psi}}_r(k).\end{aligned} \tag{6}$$

In the three-level situation, the neutral point voltage has an essential role as the currents. Aiming at balancing the voltage of the capacitor, the potential difference which shall maintain zero can be concluded by the following equation:

$$\Delta V(k+1) = \Delta V(k) + \frac{T_s}{C}\left(-\boldsymbol{i}_{abc}^T(k)\cdot\text{abs}\left(\boldsymbol{S}(k)\right)\right). \tag{7}$$

To compensate for the delay, taking one step forward to estimate the system state is of great importance. The cost function is designed in ℓ_2-norm to provide guaranteed stability [25]. In this way, the cost function of three-level NPC inverter-fed IM can be designed as

$$\begin{aligned}g_{\rm pcc} = {}& (i_{s\alpha}^* - i_{s\alpha}^p(k+2))^2 + (i_{s\beta}^* - i_{s\beta}^p(k+2))^2\\ &+ \lambda_{v1}(\Delta V^p(k+2))^2\end{aligned} \tag{8}$$

where λ_{v1} is the weighting factor for neutral point voltage.

The VV that minimizes the cost function is to be applied at the next interval.

1) Computational Effort: It is convenient for designers to develop controllers in the light of FCS-MPC. The micro controller unit (MCU), however, needs to evaluate all the possibilities online, which is a time demanding work. This problem surely hinders the development of FCS-MPC, especially, in the applications of multilevel converters and long-horizon prediction [26], in which an exponential increase in computational time is expected.

2) Stability Issue: The analysis of stability is still an open question concerning FCS-MPC. As it is addressed in [27], no closed-loop form expressions are usually seen in the FCS-MPC controllers. Even though the infinite horizon provides closed-loop stability, the horizontal-one situation cannot offer a clear approach, which complicates the analysis [28]. Sensor noises and parameter variation result in the malfunction of the controller. In this case, the suboptimal vector instead of the optimal one might be chosen.

B. Passivity-Based Control

The designing of the passivity-based controller is involved in two steps, i.e., power shaping and damping injection. Many systems, which do not contain energy sources, can be described by the Euler–Lagrange (EL) equation [23].

With system state $\boldsymbol{x}$ and input $\boldsymbol{u}$, EL equation is written as

$$\mathcal{M}\dot{\boldsymbol{x}} + \mathcal{J}\boldsymbol{x} + \mathcal{R}\boldsymbol{x} = \boldsymbol{u} \tag{9}$$

TABLE III
SIMILARITIES AND DIFFERENCES OF PBC AND PCC

	PBC	PCC
Similarities	Euler-Lagrange Function Rotor Flux Orientation	
Differences	Stability Focused Global Information Power Shaping & Damping Injection	Performance Focused Local Information Trajectory Tracking & Exhaustive Search

where $\mathcal{M}$ is a positive definite matrix, $\mathcal{J}$ is an interconnection matrix that satisfies $\mathcal{J} = -\mathcal{J}^T$, and $\mathcal{R}$ is a damping matrix.

Assigning the state $\boldsymbol{x} = [\boldsymbol{i}_s \quad \boldsymbol{\psi}_r \quad \omega_m]^T$ and input $\boldsymbol{u} = [\boldsymbol{v}_s - \boldsymbol{v}_b \quad \boldsymbol{i}_s \quad T_l]^T$, we rewrite the IM model

$$\boldsymbol{u} = \underbrace{\operatorname{diag}(\boldsymbol{O}_2, \frac{\omega_e T_r}{-L_m}\boldsymbol{J}_2, \boldsymbol{O}_2)}_{\mathcal{J}}\boldsymbol{x} + \underbrace{\operatorname{diag}(R_\sigma \boldsymbol{I}_2, \frac{1}{L_m}\boldsymbol{I}_2, B\boldsymbol{I}_2)}_{\mathcal{R}}\boldsymbol{x} + \underbrace{\operatorname{diag}(\sigma L_s \boldsymbol{I}_2, \frac{T_r}{L_m}\boldsymbol{I}_2, J\boldsymbol{I}_2)}_{\mathcal{M}}\dot{\boldsymbol{x}} \tag{10}$$

where $\boldsymbol{O}_2$ is a two-by-two zero matrix. The back electromotive force $\boldsymbol{v}_b = -k_r(\frac{1}{\tau_r}\boldsymbol{I}_2 - \omega_e \boldsymbol{J}_2)\hat{\boldsymbol{\psi}}_r$ is considered constant during a sampling period.

Designating error $\boldsymbol{x}_e = \boldsymbol{x}^* - \boldsymbol{x}$ yields

$$\mathcal{M}\dot{\boldsymbol{x}}_e + \mathcal{J}\boldsymbol{x}_e + \mathcal{R}\boldsymbol{x}_e = -\boldsymbol{u} + \mathcal{M}\dot{\boldsymbol{x}}^* + \mathcal{J}\boldsymbol{x}^* + \mathcal{R}\boldsymbol{x}^*. \tag{11}$$

To ensure the asymptotic convergence character, damping network $\mathcal{R}_i\boldsymbol{x}_e$ is added on both sides of (11)

$$\mathcal{M}\dot{\boldsymbol{x}}_e + (\mathcal{J} + \mathcal{R}_d)\boldsymbol{x}_e = -\boldsymbol{u} + \mathcal{M}\dot{\boldsymbol{x}}^* + (\mathcal{J} + \mathcal{R})\boldsymbol{x}^* + \mathcal{R}_i\boldsymbol{x}_e \tag{12}$$

where $\mathcal{R}_d = \mathcal{R} + \mathcal{R}_i$.

When the system is stable, the left-hand side of (12) converges to zero, which leads to

$$\boldsymbol{u} = \mathcal{M}\dot{\boldsymbol{x}}^* + (\mathcal{J} + \mathcal{R})\boldsymbol{x}^* + \mathcal{R}_i\boldsymbol{x}_e \tag{13}$$

Thus, the optimal VV of PBC can be obtained by solving (13).

IV. PASSIVITY-BASED MODEL PREDICTIVE CONTROL

Similar equations, though, these two schemes originate from different theories and focus on different aspects of control. FCS-MPC concentrates on the performance of reference tracking and PBC prefers the stability of the system. To alleviate the problem of computational burden and enhance its stability, a PB-MPC algorithm is proposed by injecting the concepts of PBC into the designing of the FCS-MPC method.

A. Fundamentals of PB-MPC

As we can see from Table III, FCS-MPC and PBC are both formulated based on the EL equation and many characters are complementary. To verify the feasibility, the basic structures of both schemes are reviewed.

For PBC, the optimal voltage which is calculated using speed reference and measured current with the virtual model is fed to space vector modulation (SVM). The virtual model of IM is organized by power shaping and damping injection. Because the SVM can produce most of the vectors within the hexagon plane in one sampling period, the voltage calculated by PBC is named as unconstrained voltage $\boldsymbol{v}_s^{\text{unc}}$ in this article.

For MPC, the next state of each VV is predicted with the actual model of IM. The VV that makes predictive variables approach their references in Euclidean distance is applied to the converter directly in an entire sampling period.

The proposed scheme is established on the assumption that the virtual circuit of PBC fits the prediction procedure of MPC. Based on that, the section is determined online according to $\boldsymbol{v}_s^{\text{unc}}$ calculated, in which the admissible VVs are compared with $\boldsymbol{v}_s^{\text{unc}}$. The expected performance is that the stability of the MPC is enhanced and the computational burden is reduced.

B. Proposed PB-MPC

Divide (13) into three parts, i.e., the current equation with electromotive force input, the flux equation with magnetomotive force input, and the speed equation with load torque input. With the damping resistance R_i in network $\mathcal{R}_i$, the electrical subsystem is described as

$$\boldsymbol{v}_s^{\text{unc}}(k) = R_\sigma \boldsymbol{i}_s^*(k) + \sigma L_s \dot{\boldsymbol{i}}_s^*(k) + \boldsymbol{v}_b(k) + R_i\left(\boldsymbol{i}_s^*(k) - \hat{\boldsymbol{i}}_s(k)\right) \tag{14}$$

where $\dot{\boldsymbol{i}}_s^*(k) = (\boldsymbol{i}_s^*(k+1) - \boldsymbol{i}_s^*(k))/T_s$.

Replacing the current term $\boldsymbol{i}_s^* - \boldsymbol{i}_s^p$ in (8) with voltage form $\boldsymbol{v}_s^{\text{unc}} - \boldsymbol{v}_s^p$, the cost function is modified as

$$g_{pb} = (v_{s\alpha}^{\text{unc}} - v_{s\alpha}^p(k+2))^2 + (v_{s\beta}^{\text{unc}} - v_{s\beta}^p(k+2))^2 + \lambda_{v2}(\Delta V^p(k+2))^2. \tag{15}$$

Note that the weighting factors for neutral point potential λ_{v1} and λ_{v2} are different with cost function.

The candidate region R_c is selected according to the section in which $\boldsymbol{v}_s^{\text{unc}}$ lies. In [16] and [17], the triangle candidate region (TCR) and hexagon candidate region (HCR) are introduced. The region is redrawn in Fig. 3 simply, where the blue area indicates the search region R_c and arrow presents $\boldsymbol{v}_s^{\text{unc}}$. The VVs within R_c are to be compared with $\boldsymbol{v}_s^{\text{unc}}$ in the cost function. The one that minimizes (15) is the optimal vector $\boldsymbol{v}_s^{\text{opt}}$ to be applied.

The overall diagram can be referred to in Fig. 2 and detailed PB-MPC law is shown in Algorithm 1.

Note that, due to the limitation of one vector per sampling, the FCS-MPC controller cannot generate $\boldsymbol{v}_s^{\text{unc}}$ within one sampling period. Considering the unavoidable quantization error $\boldsymbol{v}_s^{\delta}$, $\boldsymbol{v}_s^{\text{opt}}$ is expressed as

$$\boldsymbol{v}_s^{\text{opt}}(k) = \boldsymbol{v}_s^{\text{unc}}(k) + \boldsymbol{v}_s^{\delta}(k) \tag{16}$$

which is related to the current in the next step $\boldsymbol{i}_s(k+1)$ through the actual system model (5).

Even though $\boldsymbol{v}_s^{\text{unc}}$ guarantees stability, the existence of $\boldsymbol{v}_s^{\delta}$ still poses a threat to the controller.

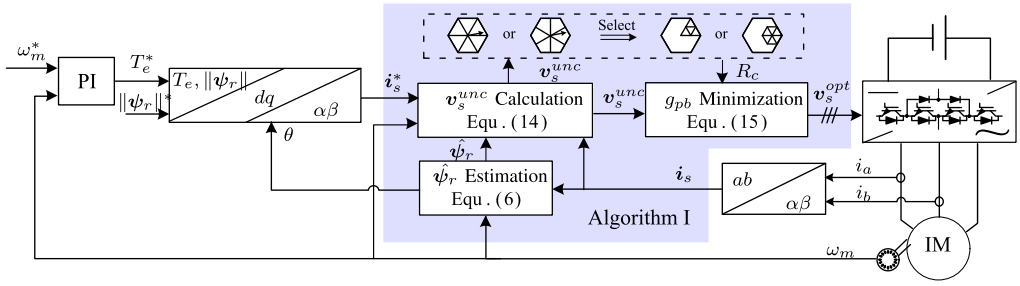

Fig. 2. Overall structure of the proposed PB-MPC.

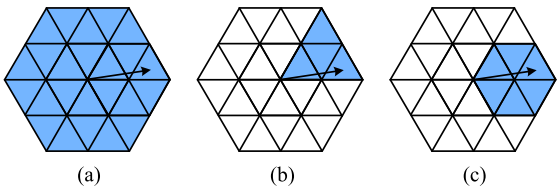

Fig. 3. Candidate regions (only one zero vector is concerned). (a) Plane of 25 vectors. (b) TCR of 8 vectors. (c) HCR of 10 vectors.

TABLE IV
QUALITATIVE EVALUATION OF EFFICIENCY OF FCS-MPC AND PB-MPC

Items	FCS-MPC	PB-MPC
Delay Compensation	1	1
Reference Current Calculation	1	1
Unconstrained Voltage Calculation	0	1
Section Selection	0	1
Iteration	25	8 or 10

Algorithm 1: Passivity-Based Model Predictive Control.

Initialization: cost $= \infty$
function $\boldsymbol{v}_s^{\text{opt}} = \text{PB-MPC}\boldsymbol{i}_s^*, \boldsymbol{i}_s, \omega_m$
$\hat{\boldsymbol{\psi}}_r$ Estimation ▷ See (6)
$\boldsymbol{v}_s^{\text{unc}}$ Calculation ▷ See (14)
R_c Selection based on $\boldsymbol{v}_s^{\text{unc}}$
for each $\boldsymbol{v}_s^p \in R_c$ **do**
ΔV Calculation ▷ See (7)
g_{pb} Minimization ▷ See (15)
if $g_{pb} <$ cost **then**
cost $= g_{pb}$
$\boldsymbol{v}_s^{\text{opt}} = \boldsymbol{v}_s^p$
end if
end for
end function
Update: $\boldsymbol{v}_s^{\text{opt}}$

V. STABILITY AND EFFICIENCY ANALYSIS

In this section, the stability of the proposed PB-MPC is proved by Lyapunov function and the efficiency can be verified in a qualitative manner, which is further tested by simulation and experimental results.

A. Efficiency

From Algorithm 1, it is known that the PB-MPCs add the segments of unconstrained voltage $\boldsymbol{v}_s^{\text{unc}}$ calculation and section R_c determination which charge the MCU additional resources. However, only 8 or 10 iterations are required for TCR and HCR each time, respectively, while FCS-MPC scrutinizes 25 possibilities.

Table IV shows a qualitative evaluation of the efficiency of FCS-MPC and PB-MPC by comparing the times that each item requires to precede. Extracting the current prediction from exhaustive search and converting it to the calculation of unconstrained voltage, the computational burden of PB-MPC is less than the FCS-MPC.

B. Stability

Because the exhaust searching is used to track reference, no explicit transfer function can be found for the control loop of FCS-MPC schemes. Thus, methods based on zero-pole analysis are hard to implement. The Lyapunov function does not need the transfer function to prove the stability of a system that is used in the stability analysis of FCS-MPC.

A positive definite Lyapunov function is designed as

$$L = \frac{1}{2}\|\boldsymbol{i}_s^* - \boldsymbol{i}_s(k)\|_2^2. \tag{17}$$

As the function indicates, this Lyapunov function is related to the Euclidean distance between the desired and actual current.

The derivative of the Lyapunov function is

$$\dot{L} = -\dot{\boldsymbol{i}}_s(k)^T \cdot (\boldsymbol{i}_s^* - \boldsymbol{i}_s(k)). \tag{18}$$

With the model of IM, (18) can be modified as

$$\dot{L} = -\frac{(\boldsymbol{v}_s^{opt}(k) - R_\sigma \boldsymbol{i}_s(k) - \boldsymbol{v}_b(k))^T}{\sigma L_s} \cdot (\boldsymbol{i}_s^* - \boldsymbol{i}_s(k)). \tag{19}$$

Substituting (14) and (16) into (19), we obtain

$$\dot{L} = -\frac{\left((R_i + R_\sigma)(\boldsymbol{i}_s^* - \boldsymbol{i}_s(k)) + \boldsymbol{v}_s^\delta(k)\right)^T}{\sigma L_s} \cdot (\boldsymbol{i}_s^* - \boldsymbol{i}_s(k)) - \dot{\boldsymbol{i}}_s^*(k)^T \cdot (\boldsymbol{i}_s^* - \boldsymbol{i}_s(k)) \tag{20}$$

For an IM whose maximum frequency is 50 Hz, $\dot{\boldsymbol{i}}_s^*$ can be taken as zero during a sampling window.

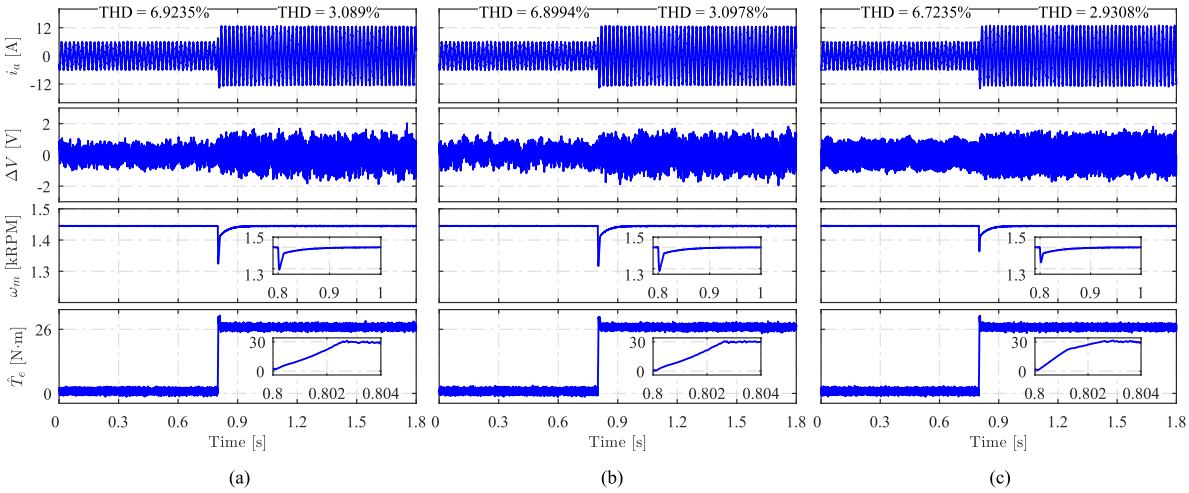

Fig. 4. Simulation results: Performance at 1445 r/min and 26 N·m with noise injected to feedback signals. (a) FCS-MPC. (b) CE-MPC with HCR. (c) PB-MPC with HCR.

To ensure global asymptotic stability, the minimum damping resistance $R_{i,\min}$ is chosen according to the following inequality:

$$(R_\sigma + R_i)\|\boldsymbol{i}_s^* - \boldsymbol{i}_s(k)\|_{-\infty} > \|\boldsymbol{v}_s^\delta\|_\infty. \tag{21}$$

Note that a damping factor too large will result in chattering problems; thus, the suggested range is $\left[R_{i,\min}, \quad 1.6R_{i,\min}\right]$. The minimum distance $\|\boldsymbol{i}_s^* - \boldsymbol{i}_s(k)\|_{-\infty}$ can be obtained by $\|\boldsymbol{i}_s^* - \boldsymbol{i}_s(k)\|_{-\infty} \approx \frac{\Delta i}{2}$, where $\frac{\Delta i}{2}$ is the current ripple. And from the point of view of geometry aspect, as shown in Fig. 3, $\|\boldsymbol{v}_s^\delta\|_\infty$ reaches its maximum values which are $\frac{2\sqrt{3}}{9}V_{\rm dc}$ and $\frac{1}{3}V_{\rm dc}$ for TCR and HCR, respectively, when $\boldsymbol{v}_s^{\rm unc}$ locates at the center of each region. This value explains the different performances between computational efficiency MPC (CE-MPC) with TCR and that with HCR in [17].

Although the damping resistance complicates the control scheme, the algorithm does show the potential of further investigation because of the merits of better performance, stronger robustness, and less computational effort.

VI. Simulation and Experimental Results

The control performance of PB-MPC is verified by simulation and experimental results based on three-level NPC converter-fed IM. Because of the ideal environment of simulation, the efficiency is not to be discussed in simulation.

The sampling time in both the simulation and the experiment is 50 μs for all algorithms. System parameters in Δ connection are shown in Table II.

For a fair comparison, the weighting factor for FCS-MPC and PB-MPC is selected in trial and error manner to achieve similar neutral point potential performance and all algorithms share the same PI controller in the speed loop.

A. Simulation Results

The comparison of FCS-MPC, CE-MPC, and PB-MPC both with HCR is carried out by MATLAB/Simulink toolbox.

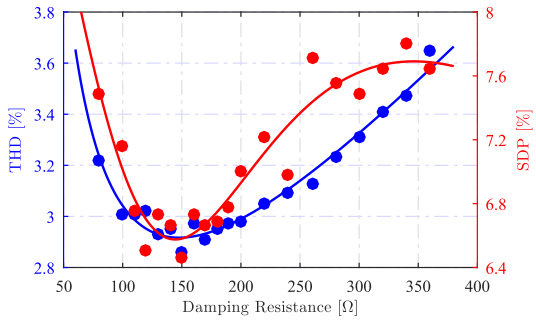

Fig. 5. Simulation results: THD and SDP. Dots present simulation results and the lines indicate the trend provided by curve fitting.

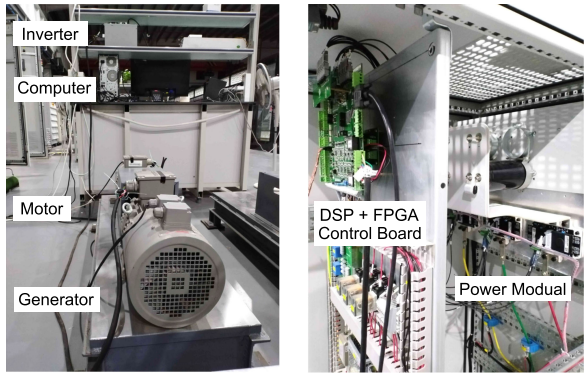

Fig. 6. Experimental setup. (a) 4-kW induction motor and inverter. (b) Control and power circuits.

The first simulation is built to verify the performance in the environment with measuring noise.

The damping resistance in this simulation is 180 Ω. To simulate the disturbance in measuring, a set of white Gaussian noise, whose energy is 17 dBm, is injected to the measured ac currents, and dc voltage signals is fed to the controllers. The curves are plotted in Fig. 4. Unlike the CE-MPC for PMSG whose performance is deteriorated in the trade of efficiency, the

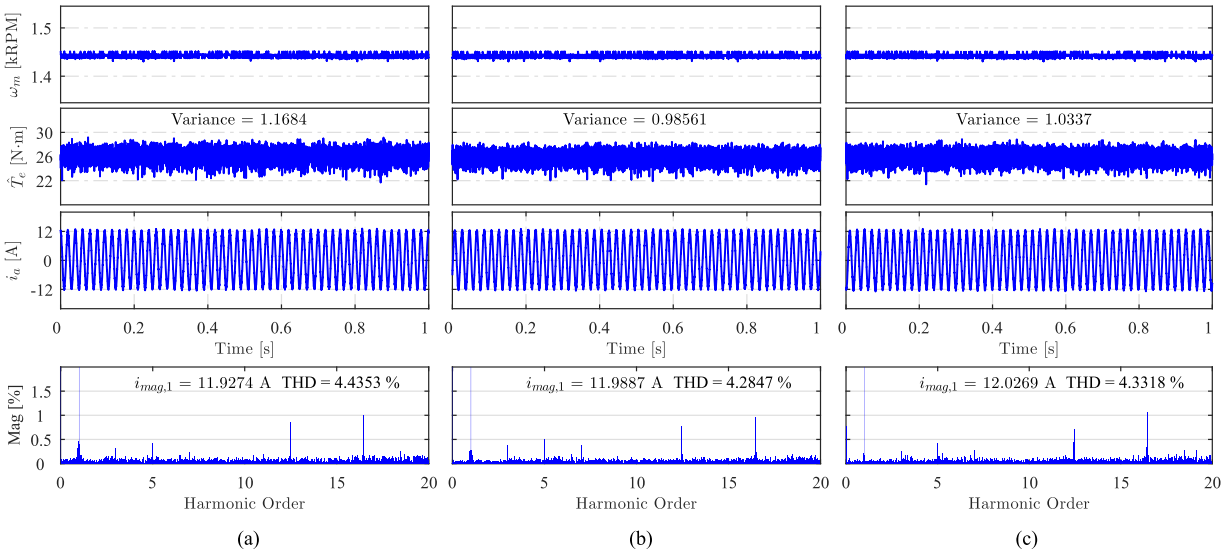

Fig. 7. Experimental results: Steady-state performance at 1445 r/min and 26 N·m with medium precision current and voltage sensor ($i_{\text{mag},1}$ denotes the magnitude of fundamental wave). (a) FCS-MPC. (b) PB-MPC with TCR. (c) PB-MPC with HCR.

CE-MPC and FCS-MPC for IM have similar performance both in loaded and unloaded. And PB-MPC has a slight improvement in the current, whose THDs are 6.72% and 2.93% in no-load and full-load, respectively. The torque response is also improved and results in a speed drop of 105 r/min; in the meantime, the FCS-MPC and CE-MPC have over 120 r/min fall in speed. The response is mainly the result of damping injection which enables faster convergence by modifying the dissipation function of the system [24].

The next simulation aims to provide an intuitive view of the influence of damping resistance exerted on the current quality and speed response. Fig. 5 shows the analysis of PB-MPC with HCR at rated speed and torque.

The speed drop ω_d is defined as the difference between the rated speed and the peak speed at full torque step, and the speed drop percentage (SDP) is calculated by $\frac{\omega_d}{1500\text{r/min}} \cdot 100\%$ which is depicted in red. Both blue and red lines are obtained by curve fitting. It can be seen that both curves present U-shape to some degree, whose minimum value is achieved at 150-Ω damping resistance simultaneously. When the damping smaller than 100 Ω is implemented, the system is not stable, and the THD and SDP increase drastically with the decreasing of injection resistance. The SDP rises more quickly than the THD and converges to 7.6% which is similar to the SDP of FCS-MPC, while the THD is growing at a certain rate.

B. Experimental Results

The MCU in the test bench is a digital signal processor (DSP) TMS320F28335 with the system clock of 150 MHz. Fig. 6 shows the experimental setup.

Current, voltage, and speed measured by the high precision sensor, torque, and flux plotted in this section are estimated values using the real model of IM with measured signals. Signals captured by oscilloscope are transferred to MATLAB for plotting and further analysis.

On experiments, the efficiency of PB-MPCs with TCR and HCR whose damping resistance is 200 Ω, are compared with those of CE-MPC, and the performance of the proposed scheme is compared with FCS-MPC due to the performance deterioration of the CE-MPC.

1) Performance at Disturbances: The performances of steady state at 1445 r/min and 26 N·m with medium precision sensors are demonstrated in Fig. 7, in which the amplitude of the currents is the rated value of 12 A. From the torque and current, we know that the performance of PB-MPC with HCR is also better than FCS-MPC, which confirms the results obtained in simulation. The PB-MPC with TCR whose THD is 4.28% and variance of torque is 0.99 outperforms the HCR at this set of injecting resistors.

Figs. 8 and 9 show current performance with high precision sensors at 1445 r/min and 13 N·m.

From the current and its THD in Fig. 9, we know that the performance of the proposed algorithm is not sacrificed in the ideal environment. Note that there still exist noises even when the high precision transducer is used.

To simulate the increasing rotor resistance in the actual motor, rotor resistance defined in DSP $\tilde{R}_r$ decreases as

$$\tilde{R}_r = (1 - 0.3t)\, R_r. \tag{22}$$

The robustness test results are shown in Fig. 8, where the estimated torque and flux are not shown due to the mismatched parameter and only the measured variables are depicted.

As we can see from the current and speed, when $\tilde{R}_r$ deviates from its nominal value R_r, the amplitude of the currents grows from 7.4 to 11.5 A gradually to meet the requirements of the soaring resistance in the virtual machine defined by the mismatched parameter. The frequencies decrease with the speed after the amplitudes of current stop changing. The FCS-MPC

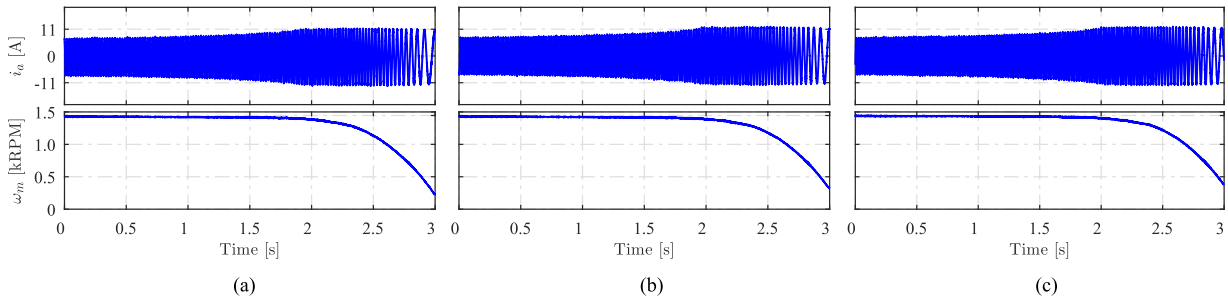

Fig. 8. Experimental results: Robust test with high precision transducer and mismatched rotor resistance $\tilde{R}_r$ at 1445 r/min and 13 N·m. (a) FCS-MPC. (b) PB-MPC with TCR. (c) PB-MPC with HCR.

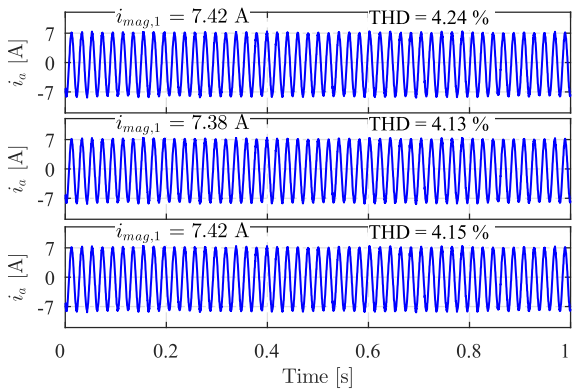

Fig. 9. Experimental results: Steady state with high precision transducer at 1445 r/min and 13 N·m. From top to bottom: FCS-MPC, PB-MPC with TCR, and PB-MPC with HCR.

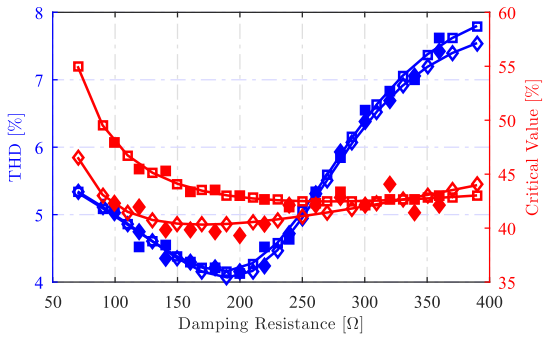

Fig. 10. Experimental results. THD and critical value in percentage of R_r. Solid dots present experimental results and the lines with empty dots indicate the trend provided by curve fitting. (Square and diamond dots denote PB-MPC with TCR and HCR, respectively.)

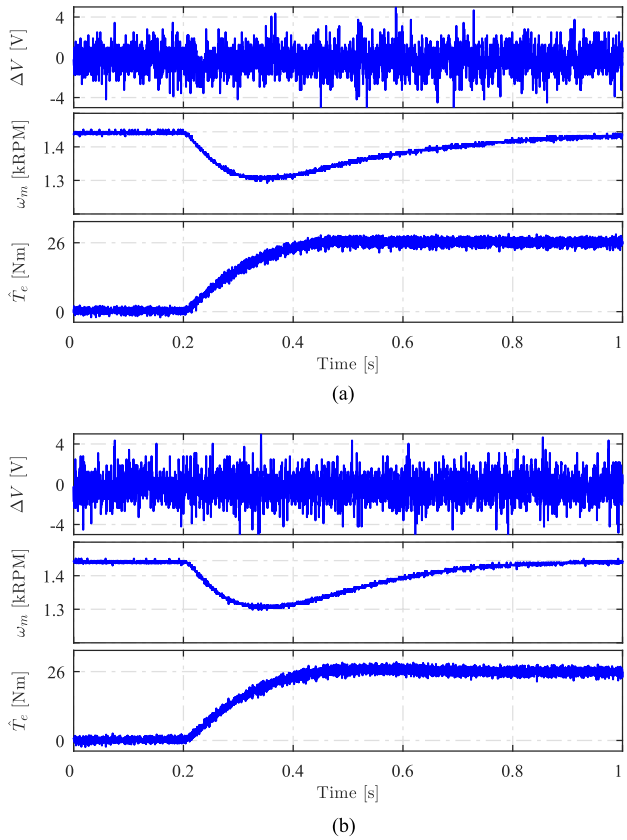

Fig. 11. Experimental results: Load torque response of 26 N·m at 1445 r/min. (a) FCS-MPC. (b) PB-MPC with HCR.

whose critical value is 44.17% of R_r suffers more from the deviated resistance, and PB-MPC with HCR which obtains stronger ability against parameter variation maintains the speed until $\tilde{R}_r$ touches 39.34% R_r.

The trend with damping resistance is drawn in Fig. 10. The same damping factor results in much the same THD for PB-MPC with TCR and HCR.

From the critical value, we find that the robustness of PB-MPC with HCR whose critical value is lower is stronger than the TCR.

Due to the limitation of the frequency converter, the ideal torque step cannot be repeated in experiments. Different from the step torque response in the simulation, the load torque response in the experiment requires more time to converge, which is given in Fig. 11. But the advantage of convergence time is preserved, as we can see from the curves of speed, the FCS-MPC requires 1 s to converge to 1445 r/min and PB-MPC needs 0.8 s when the neutral point voltage keeps the same.

Fig. 12 demonstrates the speed reversion performance from 1445 to 1445 r/min without load. The speed reference reverts at 0.3 s and the torque changes quickly to meet the needs of fast speed reversion. The flux in the $\alpha\beta$ frame acts fast and

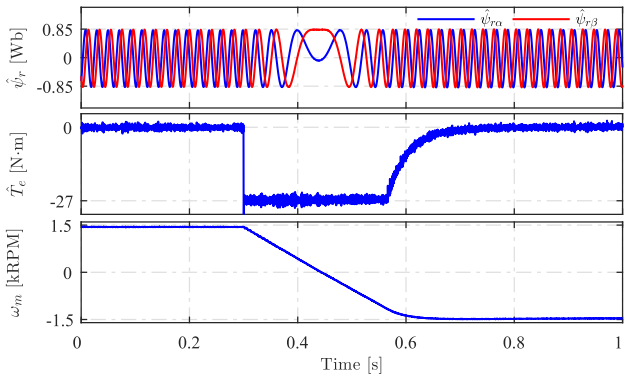

Fig. 12. Experimental results: Speed reversion from 1445 to 1445 r/min without load.

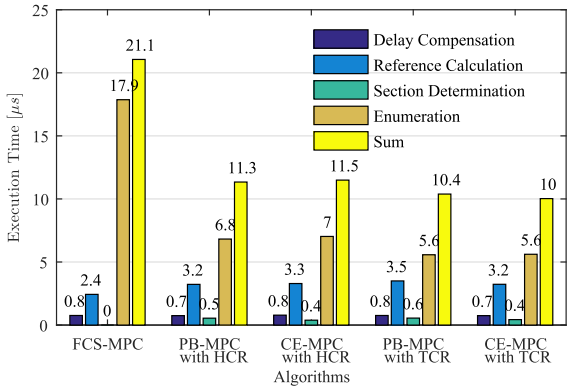

Fig. 13. Experimental results: Average execution times of each module and scheme.

smoothly as well. It takes 0.34 s to complete speed reversion without overshoot.

2) Efficiency: A bar chart is depicted in Fig. 13 according to the time consumed to indicate the time consumed by each item and algorithm. The demands from delay compensation are the same for all algorithms. The FCS-MPC spends most time searching for the optimal vector among the candidate plane of 25 VVs. Two additional stages, i.e., sector selection and unconstrained voltage calculation, which take about 1.5 μs are required, though, the overall time elapsed is reduced because the candidate set is refined according to $\boldsymbol{v}_s^{\text{unc}}$.

The total execution times are 21.06, 10.39, and 11.34 μs for FCS-MPC, PB-MPC with TCR, and PB-MPC with HCR, respectively. We can conclude from the results that the PB-MPCs with TCR and HCR reduce the computational effort by 50.68% and 46.15%, respectively, which are the same as the CE-MPC.

Triangular candidate set exceeds the hexagon candidate set when it comes to the computational burden, thanks to its fewer candidates of eight VVs.

VII. Conclusion

Aiming at alleviating the influence of sensor noises and parameter variation exerted on the FCS-MPC and reducing the computation burden, a PB-MPC is proposed in this article. By introducing the concept of PBC into the predictive controller, the performance and stability of the system are guaranteed, thanks to the virtual model deduced by power shaping and damping injection. The unconstrained VV calculated by PBC is used to locate the section where the optimal VV lies.

The stability of the proposed scheme can be verified by the Lyapunov function. Both simulation and experimental results in three-level NPC converter-fed IM confirm the ability against the disturbances from the environment and the reduction of the calculation period. The steady-state performance is improved because of the attenuation of the impacts caused by the noises and the mismatched parameters. And the computational burden is also reduced, which enables shorter sampling time or other sophisticated schemes implemented in real-time processors. Future work will focus on the PB-MPC scheme in electrolytic capacitor-less drive systems.

References

[1] P. Alemi, Y.-C. Jeung, and D.-C. Lee, "DC-link capacitance minimization in t-type three-level ac/dc/ac PWM converters," *IEEE Trans. Ind. Electron.*, vol. 62, no. 3, pp. 1382–1391, Mar. 2015.

[2] R. Selvaraj, K. Desingu, T. R. Chelliah, D. Khare, and C. Bharatiraja, "Fault tolerant operation of parallel-connected 3l-neutral-point clamped back-to-back converters serving to large hydro-generating units," *IEEE Trans. Ind. Appl.*, vol. 54, no. 5, pp. 5429–5443, Sep./Oct. 2018.

[3] J. Holtz and N. Oikonomou, "Optimal control of a dual three-level inverter system for medium-voltage drives," *IEEE Trans. Ind. Appl.*, vol. 46, no. 3, pp. 1034–1041, May/Jun. 2010.

[4] Z. Zhang, H. Fang, F. Gao, J. Rodriguez, and R. Kennel, "Multiple-vector model predictive power control for grid-tied wind turbine system with enhanced steady-state control performance," *IEEE Trans. Ind. Electron.*, vol. 64, no. 8, pp. 6287–6298, Aug. 2017.

[5] Y. Zhang and C. Qu, "Model predictive direct power control of PWM rectifiers under unbalanced network conditions," *IEEE Trans. Ind. Electron.*, vol. 62, no. 7, pp. 4011–4022, Jul. 2015.

[6] A. Ayad, P. Karamanakos, and R. Kennel, "Direct model predictive current control strategy of quasi-z-source inverters," *IEEE Trans. Power Electron.*, vol. 32, no. 7, pp. 5786–5801, Jul. 2017.

[7] J. Rodriguez *et al.*, "State of the art of finite control set model predictive control in power electronics," *IEEE Trans. Ind. Inform.*, vol. 9, no. 2, pp. 1003–1016, May 2013.

[8] F. Wang, S. Li, X. Mei, W. Xie, J. Rodriguez, and R. M. Kennel, "Model-based predictive direct control strategies for electrical drives: An experimental evaluation of PTC and PCC methods," *IEEE Trans. Ind. Inform.*, vol. 11, no. 3, pp. 671–681, Jun. 2015.

[9] J. Holtz, "Advanced PWM and predictive control an overview," *IEEE Trans. Ind. Electron.*, vol. 63, no. 6, pp. 3837–3844, Jun. 2016.

[10] P. Karamanakos and T. Geyer, "Model predictive torque and flux control minimizing current distortions," *IEEE Trans. Power Electron.*, vol. 34, no. 3, pp. 2007–2012, Mar. 2019.

[11] A. A. Ahmed, B. K. Koh, H. S. Park, K.-B. Lee, and Y. I. Lee, "Finite-control set model predictive control method for torque control of induction motors using a state tracking cost index," *IEEE Trans. Ind. Electron.*, vol. 64, no. 3, pp. 1916–1928, Mar. 2017.

[12] Z. Zhang, Z. Li, M. P. Kazmierkowski, J. Rodriguez, and R. Kennel, "Robust predictive control of three-level NPC back-to-back converter PMSG wind turbine systems with revised predictions," *IEEE Trans. Power Electron.*, vol. 33, no. 11, pp. 9588–9598, Nov. 2018.

[13] J.-S. Lee and K.-B. Lee, "Predictive control of vienna rectifiers for PMSG systems," *IEEE Trans. Ind. Electron.*, vol. 64, no. 4, pp. 2580–2591, Apr. 2017.

[14] F. Wang, Z. Zhang, J. Wang, and J. Rodrguez, "Sensorless model-based PCC for induction machine," *IET Electr. Power Appl.*, vol. 11, no. 5, pp. 885–892, May 2017.

[15] S. Vazquez, J. Rodriguez, M. Rivera, L. G. Franquelo, and M. Norambuena, "Model predictive control for power converters and drives: Advances and trends," *IEEE Trans. Ind. Electron.*, vol. 64, no. 2, pp. 935–947, Feb. 2017.

[16] C. Xia, T. Liu, T. Shi, and Z. Song, "A simplified finite-control-set model-predictive control for power converters," *IEEE Trans. Ind. Inform.*, vol. 10, no. 2, pp. 991–1002, May 2014.

[17] Z. Zhang, C. M. Hackl, and R. Kennel, "Computationally efficient DMPC for three-level NPC back-to-back converters in wind turbine systems with PMSG," *IEEE Trans. Power Electron.*, vol. 32, no. 10, pp. 8018–8034, Oct. 2017.
[18] M. Habibullah, D. D. Lu, D. Xiao, and M. F. Rahman, "A simplified finite-state predictive direct torque control for induction motor drive," *IEEE Trans. Ind. Electron.*, vol. 63, no. 6, pp. 3964–3975, Jun. 2016.
[19] M. Siami, D. A. Khaburi, M. Rivera, and J. Rodrguez, "A computationally efficient lookup table based FCS-MPC for PMSM drives fed by matrix converters," *IEEE Trans. Ind. Electron.*, vol. 64, no. 10, pp. 7645–7654, Oct. 2017.
[20] L. Yan, F. Wang, M. Dou, Z. Zhang, R. Kennel, and J. Rodriguez, "Active disturbance rejection-based speed control in model predictive control for induction machines," *IEEE Trans. Ind. Electron.*, vol. 67, no. 4, pp. 2574–2584, Apr. 2020.
[21] Z. Song, Y. Tian, Z. Yan, and Z. Chen, "Direct power control for three-phase two-level voltage-source rectifiers based on extended-state observation," *IEEE Trans. Ind. Electron.*, vol. 63, no. 7, pp. 4593–4603, Jul. 2016.
[22] R. Ortega, A. Loria, P. J. Nicklasson, and H. J. Sira-Ramirez, *Passivity-Based Control of Euler-Lagrange Systems: Mechanical, Electrical and Electromechanical Applications*. Berlin, Germany: Springer, Jun. 2013.
[23] M. M. Namazi, S. M. S. Nejad, A. Tabesh, A. Rashidi, and M. Liserre, "Passivity-based control of switched reluctance-based wind system supplying constant power load," *IEEE Trans. Ind. Electron.*, vol. 65, no. 12, pp. 9550–9560, Dec. 2018.
[24] J. Zeng, Z. Zhang, and W. Qiao, "An interconnection and damping assignment passivity-based controller for a dc–dc boost converter with a constant power load," *IEEE Trans. Ind. Appl.*, vol. 50, no. 4, pp. 2314–2322, Jul./Aug. 2014.
[25] P. Karamanakos, T. Geyer, and R. Kennel, "On the choice of norm in finite control set model predictive control," *IEEE Trans. Power Electron.*, vol. 33, no. 8, pp. 7105–7117, Aug. 2018.
[26] B. Stellato, T. Geyer, and P. J. Goulart, "High-speed finite control set model predictive control for power electronics," *IEEE Trans. Power Electron.*, vol. 32, no. 5, pp. 4007–4020, May 2017.
[27] J. A. Primbs, V. Nevisti, and J. C. Doyle, "Nonlinear optimal control: A control Lyapunov function and receding horizon perspective," *Asian J. Control*, vol. 1, no. 1, pp. 14–24, Oct. 1999.
[28] R. P. Aguilera and D. E. Quevedo, "Predictive control of power converters: Designs with guaranteed performance," *IEEE Trans. Ind. Inform.*, vol. 11, no. 1, pp. 53–63, Feb. 2015.

Fengxiang Wang (Senior Member, IEEE) was born in Jiujiang, China, in 1982. He received the B.S. degree in electronic engineering and the M.S. degree in automation from Nanchang Hangkong University, Nanchang, China, in 2005 and 2008, respectively, and the Ph.D. degree from the Institute for Electrical Drive Systems and Power Electronics, Technische Universitaet Muenchen, Munich, Germany, in 2014.

Currently, he is working as Full Professor and Deputy Director with the Quanzhou Institute of Equipment Manufacturing, Haixi Institutes, Chinese Academy of Sciences, China. His research interests include predictive control and sensorless control for electrical drives and power electronics.

Dr. Wang serves as IET Fellow and Associate Editor for the IEEE TRANSACTIONS ON INDUSTRIAL ELECTRONICS and IEEE TRANSACTIONS ON ENERGY CONVERSION. As General Chair, he organized *IEEE 5th International Symposium on Predictive Control of Electrical Drives and Power Electronics (PRECEDE)*.

Guiying Lin was born in 1995, in Guiyang, China. He received the B.S. degree from Guangzhou University, Guangzhou, China, in 2017, and the M.S. degree from Fuzhou University, Fuzhou, China, in 2020.

His research interests include model predictive control of power electronics and multilevel drive systems.

Yingjie He (Student Member, IEEE) received the B.S. degree in electrical engineering from the Shenyang University of Technology, Shenyang, China, in 2013, and the M.S. degree from Kyungsung University, Busan, Korea, in 2016. He is currently working toward the Ph.D. degree with the Institute for Electrical Drive Systems and Power Electronics, Technical University of Munich, Munich, Germany.

His research interests include power electronic converters and variable-speed motor drives and their control.